Femtosecond Dynamics of Solvation: Microscopic Friction and Coherent Motion in Dense Fluids

J. S. Baskin, M. Chachisvilis,† M. Gupta, and A. H. Zewail*

Arthur Amos Noyes Laboratory of Chemical Physics, California Institute of Technology, Pasadena, California 91125

Received: November 25, 1997; In Final Form: January 19, 1998

In this paper, we present detailed experimental and theoretical studies of the femtosecond dynamics of microscopic friction. The real-time rotational motion of a well-defined system of diatomic solute in monatomic solvent has been studied for two solvents ranging from gas to liquid densities. Both coherent inertial and diffusive limits of the motion and all stages in the transition between these two regimes are observed in detail. The transient anisotropies over the entire range of experimental densities and solvents are well-represented by the J-coherence bimolecular collision model presented here. This stochastic hard-sphere collision model explicitly relates the physical properties of the solvent to the anisotropy and the coefficient of rotational friction, permitting calculation of the transient anisotropy from the Enskog hard-sphere collision frequency. Friction coefficients obtained from J-coherence analysis of experimental anisotropies were compared with those from Gordon J-diffusion, and Langevin−Einstein analyses, and with the hydrodynamic range of friction. The density cutoff for applicability of diffusive or continuum treatments is such that the angular trajectory for average J in the angular velocity autocorrelation lifetime is ∼50°, while the microscopic, molecular picture of the friction can be applied from the gas to the liquid.

I. Introduction

Microscopic friction, the interaction of solvent and solute at the molecular level, plays a fundamental role in the dynamic evolution of solution-phase chemical and physical processes (see e.g. refs 1−3). Friction manifests itself by its influence on rotational and translational motion in the condensed phase, which influence may be described by solvent viscosity and its relationship to the Einstein diffusion limit of the Brownian motion. At the molecular level, the situation for rotational dynamics is represented schematically in Figure 1, where the rotation of a diatomic solute molecule in a bath of solvent particles is determined by the rate of collisions and by the effectiveness of those collisions in transferring angular momentum to or from the solute. At even moderate densities (a few atoms/nm^3), collisions in molecular fluids occur at subpicosecond intervals. With femtosecond time resolution, the rotational evolution of the solute can be precisely observed, and its dependence on solvent properties and densities can be characterized. Such measurements probe directly the nature of microscopic friction.

Theoretical models of the role of friction in controlling molecular rotation have a long history (see e.g. refs 4−9). These range from the Gordon stochastic binary-collision models (J-diffusion and m-diffusion),[8] which emphasize the molecular nature of the solvent, to hydrodynamic calculations that treat the solvent as a continuous viscous medium.[4,5,10] The assumptions underlying many treatments, however, preclude the quantitative prediction of dynamic behavior as a function of the physical nature of the solvent particles for arbitrary solvent and arbitrary solvent densities. The gradual transition of the polarization anisotropy from its distinctive and nonmonotonic free-rotor form to a diffusion-controlled exponential decay at long time and nonzero pressure is approximated in the Gordon models, although not quantitatively and without explicit solvent dependence, while other treatments are invalid under conditions of large angle free (inertial) rotation and therefore cannot reproduce the coherence associated therewith. The following question must then be asked: Can the quantitative features of the measured dynamics be captured for a broad range of densities by a simple model, short of a full molecular dynamics simulation?

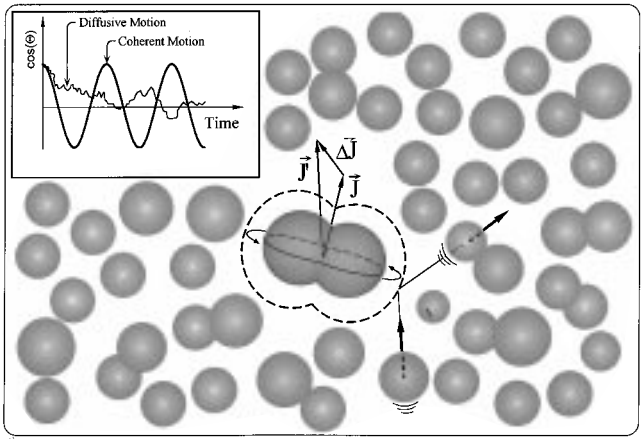

Figure 1. Schematic of the microscopic origin of friction on the rotational motion of a diatomic solute in atomic solvent. A random collision interrupts the free rotation of the diatom and causes a change $\Delta\vec{J}$ in angular momentum (from initial $\vec{J}$ to final $\vec{J}'$). In the inset, the limiting cases of diffusive and purely coherent rotation are illustrated conceptually by a plot of $\cos(\Theta(t))$, where $\Theta(t)$ is the evolution with time of the polar angle formed by the diatom internuclear axis with its direction at $t = 0$.

† Postdoctoral fellowship from the Swedish Foundation for International Cooperation in Research and Higher Education.

S1089-5639(98)00338-7 CCC: $15.00
Published on Web 03/19/1998

We recently reported[11] direct femtosecond measurements of the rotational anisotropy of iodine from isolated molecule conditions to near-liquid densities in supercritical argon and applied a binary-collision model that incorporated accurate hard-sphere atom-diatom collision dynamics, including the persistence of coherent rotational motion through many collisions (J-coherence model), to extract the density dependence of solvent friction across the full range of densities. Here we expand on that work, describing in detail the J-coherence model and examining its value in linking in a simple and direct manner the physical characteristics of the solvent particles, the rates of solvent−solute collision, and rotational friction. We also give a full account of the analysis of experiments with both helium and argon as solvent and compare with the Gordon J-diffusion model and well-known Langevin equation and hydrodynamic treatments. This problem of the diffusive motion has been the subject of many experimental and theoretical studies, and a perspective was already given in ref 11 of the work done by the groups of Berne, Chandler, Eisenthal, Hochstrasser, Hynes, and others (for reviews, see refs 1−3 and 9).

The paper is organized as follows. In section II, a review is given of the principal theoretical treatments applied to our measurements, in addition to a full development of the J-coherence model. A description of the experimental apparatus and procedures is given in section III, followed by a presentation of experimental and fitting results in section IV. The noteworthy features of those results are discussed in section V and summarized in section VI.

II. Theoretical Section

A. Definition of Terms. In attempting to illuminate the microscopic dynamics illustrated in Figure 1, we must proceed experimentally by the method of probing the macroscopic transient polarization anisotropy, $r(t)$, of a statistical sample of molecule-fixed transition dipoles. The experimental quantity is

$$r(t) = (I_{\parallel}(t) - I_{\perp}(t))/(I_{\parallel}(t) + 2I_{\perp}(t)) \tag{1}$$

where $I_{\parallel}(t)$ and $I_{\perp}(t)$ are the transient pump−probe intensities measured for probe polarization vector parallel and perpendicular, respectively, to that of the pump. This quantity can also be expressed in terms of the ensemble-averaged motion of $\hat{\mu}_2$, the probe transition dipole unit vector, with respect to the pump transition dipole, $\hat{\mu}_1$:

$$r(t) = 0.4\langle P_2[\hat{\mu}_1(0)\cdot\hat{\mu}_2(t)]\rangle \tag{2}$$

where P_2 is the second-order Legendre polynomial and $\langle ... \rangle$ denotes the ensemble average.

Another dynamic variable which characterizes the ensemble, but which is not directly measurable, is the angular velocity autocorrelation function, given by

$$\Omega(t) = \langle \vec{\omega}(t)\cdot\vec{\omega}(0)\rangle \tag{3}$$

where $\vec{\omega}$ is the angular velocity of a molecular rotor.

In the case with which we are concerned here, the B ← X pump transition and the E ← B probe transition of molecular iodine, both transition dipoles are well-defined and parallel to the internuclear axis ($\hat{\mu}_1 = \hat{\mu}_2 = \hat{\mu}$). For a linear rotor, such as diatomic iodine, the angular momentum is $\vec{J} = I\vec{\omega}$, where I is the moment of inertia. I, in turn, is equal to $^1/_4Mr^2$ for diatomic mass M and internuclear distance r. In the absence of collisions, i.e., when there is no friction (free rotation), $\vec{J}$ and $\vec{\omega}$ are conserved, and $\Omega(t)$ is a constant. In contrast, with (collisional) friction, at sufficiently long times $\vec{J}$ is randomized and $\Omega(t)$ must decay to zero. Thus, $\Omega(t)$ measures the degree of angular momentum scrambling in the sample.

The ensemble averages in eqs 2 and 3 are over the distribution of angular velocities that characterizes the sample. For a thermally equilibrated sample, this distribution is determined by the moment of inertia. It must be noted, however, that I depends on the vibronic state of the molecule, so photoexcitation can produce samples with rotational distributions that do not correspond to the ambient temperature. Equilibration through subsequent collisions then results in an evolution of the sample rotational temperature.

This situation applies for the B ← X transition of iodine. At room temperature (296 K), the ground-state rotational distribution (rotational constant $B'' = \hbar/(4\pi cI) \cong 0.037$ cm^{-1}) has a peak, given by $[kT/(2Bch)]^{1/2} - {}^1/_2$, near $J = 51$. The average internuclear separation is greater in the excited state, reducing B′ to ∼0.0275 cm^{-1}. Thus, immediately upon photoexcitation, in which J changes by at most $\hbar$, the rotational distribution corresponds to a lower temperature (220 K).

Finally, for the subsequent discussion of the interaction of solute and solvent particles, M and m will be used to refer to the mass of solute and solvent, respectively.

B. Langevin Friction Model. The purpose of this section is to quantify the concept of friction as it emerges from a derivation appropriate to the high-density limit. The relationship established between $\Omega(t)$ and the reduced coefficient of rotational friction, ξ, then serves to define fiction in the analysis of experiments at all densities.

The reorientational motion of a solute molecule in high-density fluids may be treated as a form of rotational Brownian motion. In this model, the total torque acting on the molecule is separated into the frictional torque, which is proportional to the angular velocity of the molecule, and a random torque $\vec{T}$. Such a separation can be shown to be strictly valid in the case of translational motion of a slow, heavy particle in a bath of light particles, i.e., in the limit $m/M \rightarrow 0$,[12] since in this case the expectation value of the rate of momentum transfer (force) is proportional to the velocity of the heavy particle.

The motion of a linear rotor with two rotational degrees of freedom is described by the Langevin equation for $\vec{\omega}$,

$$I\frac{\partial}{\partial t}\vec{\omega}(t) = -\xi I\vec{\omega}(t) + \vec{T} \tag{4}$$

where ξ is the *reduced friction coefficient*. (The standard friction coefficient is $\zeta = \xi I$; note that the dimension of ξ is inverse time.) It is assumed that $\vec{T}$ has the following properties:

$$\langle \vec{T} \rangle = 0 \tag{5a}$$

$$\langle \vec{T}(t_1)\cdot\vec{T}(t_2)\rangle = 2\pi T_0\delta(t_1 - t_2) \tag{5b}$$

$$\langle \vec{T}(t)\cdot\vec{\omega}(0)\rangle = 0 \tag{5c}$$

where $T_0 = (1/2\pi)\int_{-\infty}^{\infty}\langle \vec{T}(t)\cdot\vec{T}(0)\rangle\, dt$ is a spectral density of the random torque at zero frequency.

Property 5b, an infinitesimally short correlation time of the random torque, represents the limit of instantaneous dissipation. In essence, it requires that there exist a time interval Δt such that even though $\vec{\omega}(t+\Delta t) - \vec{\omega}(t)$ is small, no correlation exists between $\vec{T}(t+\Delta t)$ and $\vec{T}(t)$. It is believed that this condition is fairly insensitive to the nature of the heat bath as long as the bath consists of molecules that are much lighter than the one

under investigation. However, deviations are expected at high densities due to collective response of the bath. For example, "ring" collisions or backscattering effects will cause non-Markovian behavior which is a consequence of the fact that the system has a finite memory time.[13−16] These effects can be accounted for by using memory function formalism that introduces a time-dependent friction coefficient.[17,18] The condition 5c implies that there is no correlation between initial velocity and random torque, which is as expected for an infinitesimally short force correlation time.

Equation 4 can be integrated to yield the mean square angular velocity.[18,19] Then, using eq 5 and assuming that at a sufficiently long time the mean-square angular velocity should approach its equipartition value ($\langle|\vec{\omega}(\infty)|^2\rangle = 2kT/I$ at temperature T), one finds that the friction coefficient is related to the spectral density of random torque,

$$\xi = \frac{\pi T_0}{2kTI} \tag{6}$$

This relation is known as a fluctuation−dissipation theorem and results from the separation of the total torque on the Brownian particle into the frictional and the random parts.

Using eqs 4 and 5, it is straightforward to show that[18]

$$\Omega(t) = \frac{2kT}{I}\mathrm{e}^{-\xi t} \tag{7}$$

That is, the rate of decay of the angular velocity autocorrelation function is simply equal to the friction coefficient. The exponential decay is a consequence of Markovian properties of $\vec{T}$. In the following, we will use $t = 1/\xi$ to designate the decay time of $\Omega(t)$.

In order to calculate the experimentally observed quantity, $r(t)$, it is necessary to follow the angular motion of the dipole or, here, the rotor axis. The basic equation governing the time evolution is

$$\frac{\partial}{\partial t}\hat{\mu}(t) = \vec{\omega}(t) \times \hat{\mu}(t) \tag{8}$$

where $\vec{\omega}(t)$ is a Markovian stochastic process in our case. The formal solution is given by

$$\hat{\mu}(t) = P\mathrm{e}^{\int_0^t \mathrm{d}t' \vec{\omega}(t')\cdot\hat{R}}\hat{\mu}(0) \tag{9}$$

where P is the time ordering symbol and $\hat{R}$ represents a set of infinitesimal rotation operators.[17,20−22]

Equation 8 can only be used directly to calculate the first-order Legendre polynomial ($\hat{\mu}(t)\cdot\hat{\mu}(0)$). To obtain the second-order Legendre polynomial, this equation can be generalized for higher spherical harmonics, which leads to the following expression for the transient anisotropy:

$$r(t) = \langle \mathrm{tr}\, P\mathrm{e}^{\int_0^t \mathrm{d}t' \vec{\omega}(t')\cdot\hat{R}}\rangle \tag{10}$$

The moment expansion of eq 10 suffers from poor convergence. Accordingly, the cumulant expansion is used to obtain an approximate solution.[23] We use the second-order cumulant approximation, which leads to the expression

$$r(t) = 0.4\mathrm{e}^{-3/2\int_0^t\int_0^{t'}\langle\vec{\omega}(t')\cdot\vec{\omega}(t'')\rangle \mathrm{d}t'\mathrm{d}t''} = 0.4\mathrm{e}^{-3\int_0^t(t-s)\langle\vec{\omega}(s)\cdot\vec{\omega}(0)\rangle ds} \tag{11}$$

This is justified at very high pressures when the free rotation time of the molecules is significantly smaller than the mean thermal reorientation time. It is worth noticing that the double integral in eq 11 represents the mean-square angular deviation from the initial position.

Equation 11 relates $r(t)$ to $\Omega(t)$ and can be used to obtain $\Omega(t)$ from anisotropy data as

$$\Omega(t) = -\frac{1}{3}\frac{\mathrm{d}^2 \ln(r(t))}{\mathrm{d}t^2} \tag{12}$$

or, substituting for $\Omega(t)$ from eq 7, eq 11 can be integrated to yield the analytical expression for transient anisotropy,

$$r(t) = 0.4 \exp\left(-\frac{6kT}{I}(\tau^2\mathrm{e}^{-t/\tau} + \tau t - \tau^2)\right) \tag{13}$$

For $t \gg \tau$, the anisotropy decays exponentially,

$$r(t) = 0.4 \exp\left(-\frac{6kT}{I}(\tau t - \tau^2)\right) = C \exp\left(-\frac{6kT\tau}{I}t\right) \tag{14}$$

where the amplitude C depends on τ such that $r(t) = 0.4$ at $t = \tau$. Using the Langevin−Einstein value for the rotational diffusion constant, $D_\mathrm{r} = kT/(\xi I) = kT\tau/I$, one sees that the anisotropy decays exponentially with rate $6D_\mathrm{r}$, the well-known result for the diffusive limit. This relation defines the diffusive rotational relaxation time $\tau_\mathrm{rot} = 1/(6D_\mathrm{r})$. Note that, in this limit, the decay rate of anisotropy is *inversely* related to the decay rate ξ of $\Omega(t)$, or $\tau \propto 1/\tau_\mathrm{rot}$.

In the opposite case, at $t < \tau$ the decay of the anisotropy is Gaussian in form and *independent* of τ (or ξ):

$$r(t) = 0.4 \exp\left(-\frac{3kT}{I}t^2\right) \tag{15}$$

The motion of the solute in this regime has not yet been influenced by the solvent medium, and eq 15 is accordingly identical to the early time limit of free inertial motion at temperature T.[8] The possibility of evolving rotational temperature, such as occurs in iodine B ← X excitation, is not accounted for in these expressions.

C. Hydrodynamic Treatment. The preceding section relates the rotational dynamics of the solvent to a reduced coefficient of rotational friction, which is a property of the solute−solvent system, without prescribing how to determine the value of this coefficient. One means of attacking this problem is through hydrodynamic theory. By treating the solvent as a viscous fluid continuum and approximating the solute molecule as an ellipsoid, the coefficient of friction for rotation can be calculated as a function of the ellipsoid dimensions and shear viscosity η of the solvent. The result also depends on the boundary condition assumed at the solute−solvent interface and is valid in the same limit as the Langevin treatment; that is, for small m/M and collision time short on the time scale of free rotation. Even then, the choice of boundary condition appropriate to a particular system remains a source of uncertainty in the result.

Expressions for rotational friction of a prolate ellipsoid of revolution about an axis perpendicular to the symmetry axis, which is the case appropriate to the anisotropy of a diatom with transition dipole parallel to the internuclear axis, were taken from ref 5 for sticking boundary condition, and the ratio of slipping to sticking friction is given in ref 10. When the

ellipsoid has semimajor axis a and semiminor axis b, one finds for the reduced coefficient

$$\xi_{\text{stick}} = \frac{4\eta V}{I} \frac{1-\beta^4}{\beta^2 \frac{(2-\beta^2)}{2\sqrt{1-\beta^2}} \ln\left(\frac{1+\sqrt{1-\beta^2}}{1-\sqrt{1-\beta^2}}\right) - \beta^2} \quad (16)$$

where V is the ellipsoid volume ($V = {}^4/_3\pi ab^2$) and $\beta = b/a$. The ratio $\xi_{\text{slip}}/\xi_{\text{stick}}$ may then be found in Table 1 of ref 10 as a function of b/a (denoted there by τ). In this hydrodynamic description, the Stokes−Einstein relationship, which relates viscosity to the rotational diffusion, is usually invoked:

$$\tau_{\text{rot}} = \xi I/6kT = f\eta V/kT$$

which follows from eq 16 and the relations of the previous section. In the stick limit, the geometrical shape factor, f_{stick}, is equal to ${}^2/_3$ times the β-dependent factor in eq 16, while $f_{\text{slip}} = f_{\text{stick}}\xi_{\text{slip}}/\xi_{\text{stick}}$.

D. Gordon's J- and m-Diffusion Models. The J- and m-diffusion models[8] were developed by Gordon to overcome any restriction to small angular steps for the free rotation between collisions, which clearly limits the preceding theories to relatively high densities. In these purely collisional models, the interaction of solute and solvent results solely from discrete, Poisson-distributed events ("collisions") with collision interval τ_{coll}. Between collisions, free rotation of the rotor pertains, and arbitrarily large angular excursions under free inertial motion are possible at large τ_{coll}. These features of the Gordon models are incorporated into the J-coherence model as well. The distinction lies in how the collision affects the solute angular momentum, $\vec{J}$.

In the Gordon models, the key to obtaining a closed form solution for the polarization anisotropy is the assumption that the direction of $\vec{J}$ is randomized at each collision. In the m-diffusion model, the magnitude J remains constant, while in the J-diffusion model J is also randomized over a thermal distribution at each collision. In the early stages of this study, both the m- and J-diffusion models were studied, but the J-diffusion fitting results provided a clearly superior approximation to our data, so only J-diffusion is considered in detail here. The J-diffusion assumption is also more physically intuitive, since the magnitude of $\vec{J}$ must, in general, be randomized at least as fast as its direction, when $\Delta\vec{J}$, the collision-induced change in $\vec{J}$, is not preferentially perpendicular to $\vec{J}$.

The J-diffusion expression for polarization anisotropy is[8]

$$r(t) = 0.4e^{(-t/\tau_{\text{coll}})} \sum_{n=0}^{\infty} \frac{1}{(\tau_{\text{coll}})^n} \int_0^t F_0^{(2)}(t-t_n) \int_0^{t_n} F_0^{(2)}(t_n - t_{n-1}) \int_0^{t_{n-1}} \dots \int_0^{t_3} F_0^{(2)}(t_3 - t_2) \int_0^{t_2} F_0^{(2)}(t_2 - t_1) F_0^{(2)}(t_1)\, dt_1\, dt_2 \dots dt_{n-2}\, dt_{n-1}\, dt_n \quad (17)$$

or

$$r(t) = 0.4e^{(-t/\tau_{\text{coll}})} \sum_{n=0}^{\infty} \frac{1}{(\tau_{\text{coll}})_n} F_n^{(2)}(t) \quad (18)$$

where each term in the sum represents the contribution to the anisotropy of molecules that have undergone exactly n collisions up to time t. $F_0^{(2)}(t)$ is proportional to the transient anisotropy following optical excitation of a freely rotating linear rotor with parallel dipole $\hat{\mu}(t)$:

$$F_0^{(2)}(t) = \langle P_2(\hat{\mu}(0)\cdot\hat{\mu}(t)_{\text{free rotor}})\rangle$$

$$= 0.25 + 0.75\frac{B_x hc}{kT} \sum_J (2J+1) \times \exp\left(-\frac{B_x hcJ(J+1)}{kT}\right) \cos(8\pi B' cJt) \quad (19)$$

where B_x and B' are rotational constants of the rotor in cm^{-1} and J is the angular momentum quantum number. B_x is the rotational constant before $t = 0$, which determines the thermal J distribution, while B' reflects the rotational inertia for $t > 0$, which controls the rotational velocity.

Each $F_0^{(2)}$ function in a given term of the summation in eq 17 corresponds to motion in a specific intercollision interval. For all intervals following the first collision, the J-diffusion model postulates an equilibrated J distribution, so $F_0^{(2)}$ is calculated with $B_x = B'$. The J distribution preceding the first collision is that of the ground state, however, so B_x must be set equal to B'' when using eq 19 to calculate $F_0^{(2)}(t_1)$ in eq 17. The τ_{coll}-independent functions $F_n^{(2)}$ in eq 18 were calculated and stored for n up to 40 and then recalled and combined with the appropriate τ_{coll}-dependent weighting to calculate $r(t)$ for a given τ_{coll} in fitting the data.

The J-diffusion assumption of angular momentum randomization at each collision means that the angular velocities before and after a collision are uncorrelated ($\langle\vec{\omega}(t_{\text{coll}}^-)\rangle\cdot\vec{\omega}(t_{\text{coll}}^+)\rangle = 0$). Thus, the only contribution to the angular velocity autocorrelation function (eq 3) comes from the population which has suffered no collisions ($n = 0$). According to the Poisson distribution, this population decays exponentially with time constant τ_{coll}; that is, $\tau = \tau_{\text{coll}}$.

E. J-Coherence Model. Although the Gordon J-diffusion model reproduces the anisotropy functions at both the free rotor and the diffusion limits and provides a qualitative description of the continuous transition between those limits, there is no quantitative connection between the physical parameters of the solute−solvent system and the calculation. This disconnection arises from the assumption of complete J randomization with each collision, leading to the identification at the end of the preceding section of the J-diffusion τ_{coll} with τ, the effective angular momentum scrambling lifetime, while it is the true collision interval that is derived from kinetic gas treatments. The relationship between the two depends profoundly on the particulars of the case in question, including the masses, moment of inertia, temperature, and the intermolecular potential.

In order to establish the link between the physical parameters and the friction (i.e., decay of $\Omega(t)$), randomization of $\vec{J}$ must be replaced by an approximation of the specific distribution of final $\vec{J}$ which is produced by the dynamics of the actual binary collisions. This is done in the J-coherence model,[11] in which the general framework of the Gordon models is retained, but following the nth collision, the distribution of $\vec{J}_{n+1}$ is not thermal, but given by the function $P_{\vec{J}}(\vec{J}_n,T,m)$, which incorporates a precise classical treatment of the collision dynamics of the rotor with a solvent atom of mass m, at solvent temperature T. In addition to giving the model predictive value, the closer correspondence to reality of the derived kinetics when including the partial persistence of rotational coherence across collisions may be expected to yield quantitatively more accurate anisotropy functions.

The calculation of $P_{\vec{J}}(\vec{J}_n,T,m)$ is based upon the bimolecular collision dynamics of a solvent hard sphere impinging on a rigid-rotor molecule composed of two hard spheres at a separation r,

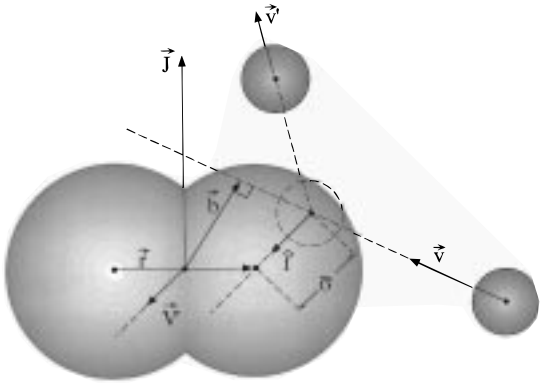

Figure 2. Diagram of a typical hard-sphere atom−diatom collision underlying the J-coherence model calculations. Quantities that are required in the calculations are labeled in the figure and defined in the text.

as illustrated in Figure 2. The collision geometry is defined in the diatom rest frame at the time of impact, in which frame the atom approaches with the relative velocity $\vec{v}$ of atom and diatom center of mass. Note that the atom is shown in Figure 2 before and after impact, while the position of the diatom is shown only at the time of impact. From conservation laws, $\Delta\vec{J}$, the collision-induced change in $\vec{J}$, can be solved analytically as a function of $\vec{J}$, the relative velocity $\vec{v}$, and impact parameter $\vec{b}$ in the molecular reference frame. The central force nature of the atom−atom interaction dictates that the impulse received by the iodine molecule is directed from the point of impact through the center of the impacted iodine atom, along unit vector $\hat{f}$ in Figure 2. Defining $\hat{r} = \vec{r}/r$ (a unit vector along the internuclear axis pointing toward the impacted iodine atom), one finds (see Appendix)

$$\Delta\vec{J} = \left(\frac{Mr(\vec{v}\cdot\hat{f}) + 2(\vec{J}\times\hat{f})\cdot\hat{r}}{2 + M/m - (\hat{r}\cdot\hat{f})^2}\right)(\hat{r}\times\hat{f}) \qquad (20)$$

where M and m are the masses of the solute molecule and solvent atom, respectively. $\hat{f}$ is given in turn by $\hat{f} = [{}^1\!/_2\vec{r} - (\vec{b} + \alpha\vec{v})]/\bar{\sigma}$, where $\bar{\sigma}$ is the atom−atom hard-sphere collision distance, and α is the time of impact relative to the time of closest proximity between atom and diatom center of mass on the hypothetical trajectory defined by the uninterrupted extension of $\vec{v}$ in Figure 2. α is determined by $\vec{v}$, $\vec{b}$, $\vec{r}$, and $\bar{\sigma}$:

$$\alpha = \frac{\vec{v}\cdot\vec{r}}{2v^2} \pm \frac{1}{v}\left\{-\left[1 - \left(\frac{\vec{v}\cdot\hat{r}}{v}\right)^2\right]\left(\frac{r}{2}\right)^2 - b^2 + \vec{b}\cdot\vec{r} + \bar{\sigma}^2\right\}^{1/2} \qquad (21)$$

Physically, the first term in eq 20 is the contribution of the center of mass relative motion of atom and diatom, while the second term represents the effect of $\vec{v}_{rot} = (J/I) \times (\vec{r}/2 - \hat{f}\bar{\sigma})$, the purely rotational component of the velocity of the collision surface at the point of impact. To highlight this fact, eq 20 may be expressed in the following alternate form:

$$\Delta\vec{J} = \left(\frac{Mr(\hat{r}\times\hat{f})}{2 + M/m - (\hat{r}\cdot\hat{f})^2}\right)(\vec{v} - \vec{v}_{rot})\cdot\hat{f} \qquad (22)$$

If $(\vec{v} - \vec{v}_{rot})\cdot\hat{f}$ is negative, the atom and surface are separating at the point of intersection of the trajectory and the collision surface, and no collision occurs. In other words, $\Delta\vec{J}$ can only be in the direction of the torque, which is also the direction of $\hat{r}\times\hat{f}$, and there is a collision only when the coefficient of $\hat{r}\times\hat{f}$ in eq 20 is positive, although either of the two contributions may be negative. For example, a negative first term and positive second term represents the collision surface rotating toward and overtaking a receding solvent atom.

There are potentially four values of α from the choice of sign in eq 21 and the two directions of $\vec{r}$, corresponding to intersections of the atomic trajectory with the collision surface for positive and negative $\vec{v}\cdot\hat{f}$ on each of the two component atoms of the solute molecule. The smallest and largest α for which the argument of the radical is positive represent trajectory entry and exit points and are both considered as possible collision geometries in the sampling process.

From the expression for $\Delta\vec{J}(\vec{J},\vec{v},\vec{b},m)$, one obtains the required distribution $P_{\vec{J}}(\vec{J},T,m)$ as the probability distribution of $\vec{J} + \Delta\vec{J}(\vec{J},\vec{v},\vec{b},m)$ when the Maxwell−Boltzmann distribution of relative velocity and corresponding appropriate distribution of impact parameter are taken into account. In practice, a sample from $P_{\vec{J}}(\vec{J},T,m)$ is found numerically by randomly sampling from the $\vec{v}$ and $\vec{b}$ distributions and applying eq 20, with an additional weighting of collision geometries by the total effective relative velocity at impact (v_{rel}^{eff}), including $\vec{v}_{rot}$ of the collision surface for a rotating diatom. This last effect induces also a J dependence of the total collision probability, which is recorded separately from the $P_{\vec{J}}(\vec{J},T,m)$ samples. The anisotropic collision cross section is accounted for by sampling b over a fixed area for all directions of $\vec{v}$.

To determine the time evolution of both the anisotropy and the angular velocity autocorrelation function of the thermal sample at collision frequency $1/\tau_{coll}$, rotational trajectories of a large number of diatoms (here, 100 000) are recorded at time steps no larger than $0.04\tau_{coll}$, with free rotation at fixed $\vec{J}$ interrupted by Poisson distributed collisions, adjusted for the J-dependent total cross-section factor. A new $\vec{J}$ is then selected from $P_{\vec{J}}(\vec{J},T,m)$ which determines the evolution until the next collision.

In the lab frame, the distribution of atomic velocity, $\vec{v}_a$, is spatially uniform and isotropic with respect to the internuclear axis, and $\vec{b}$ is uniformly distributed in the plane perpendicular to $\vec{v}_a$, while $\vec{v} = \vec{v}_a - \vec{V}$ is anisotropically distributed for nonzero diatom velocity, $\vec{V}$. The rigorous expression for v_{rel}^{eff} in the limit of infinitesimal $d\vec{v}_a$ is $v_{rel}^{eff} = [v_a/(\vec{v}_a\cdot\hat{f})](\vec{v} - \vec{v}_{rot})\cdot\hat{f}$. However, by including $\vec{V}$ explicitly in the calculation, the distribution $P_{\vec{J}}(\vec{J},T,m)$ averaged over V was found to differ negligibly from the calculation for isotropic $\vec{v}$, while V and J where also uncorrelated over the range of populated V. Therefore, the final anisotropy simulations were simplified by removing explicit dependence on V. Also, because the evaluation of the collision geometry is limited to the instant of impact only, some collisions will be included in which the iodine and rare gas atom may overlap at an earlier or later point in their free particle motion. The correlations implied by such trajectories are rare except at very high rotational velocities and are ignored. These two approximations greatly reduce the time and complexity of the calculations.

The implementation of the equations for binary collision (eq 20 and related equations in the appendix for changes in $\vec{v}$ and $\vec{V}$) was checked for energy and linear and angular momentum conservation. To test sampling in the final anisotropy calculations, both the time-averaged J distribution for a single iodine, and the ensemble average after many collisions were confirmed to be close to Boltzmann (within 2%) independent of collider mass. For calculations in which the iodine velocity was tracked, its time average after many collisions was also within 2% of the theoretical value.

From the J-coherence calculations, both the anisotropy and $\Omega(t)$ are obtained. $\Omega(t)$ is single exponential in form, and its

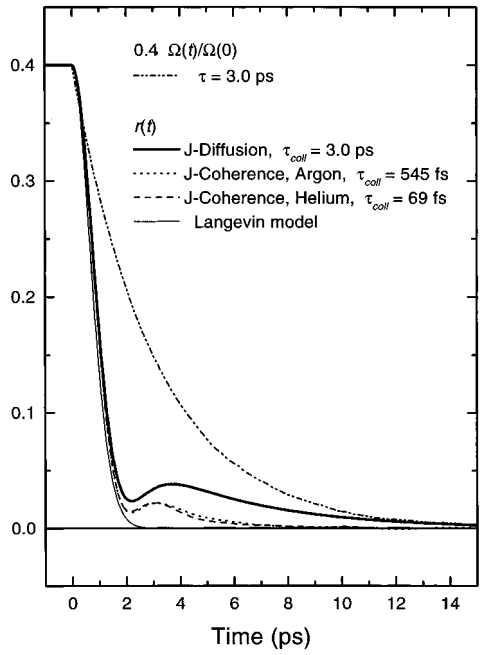

Figure 3. Theoretical anisotropy decays of iodine which correspond to angular velocity autocorrelation functions with a single decay rate $1/\tau$, where $\tau = 3$ ps. Comparison of J-coherence of iodine in argon and in helium, with J-diffusion and Langevin treatments (no solvent dependence). The exponential decay of the angular velocity autocorrelation function $\Omega(t)$ of all four is also shown. Here, the Langevin model deviates at early time since a constant rotational temperature of 296 K has been assumed. The other models incorporate rotational equilibration starting from the initial ground-state distribution.

lifetime τ can be compared with τ_{coll} to quantify the J scrambling potency per collision of each solvent. It is found that, for the parameters used here in the J-coherence model ($M = 253.8$ amu, $r = 3.11$ Å, the average separation of the iodine nuclei for $v = 9$ in the B state, $T = 296$ K, and $\bar{\sigma} = 3.52$ Å for iodine−argon and 3.07 Å for iodine−helium, from the $^1/_2kT$ turning points of I atom−rare gas potentials found in the literature[24,25]), τ is proportional to τ_{coll} with proportionality constants of 5.5 for argon and 43 for helium. That is, the angular velocity of an average iodine molecule persists through ~5.5 collisions with argon and 43 collisions with helium.

In Figure 3 are shown the theoretical J-coherence and J-diffusion anisotropy decays of iodine in argon and in helium which correspond to a single value of τ of 3.0 ps. The (scaled) angular velocity autocorrelation function is also plotted. For J-diffusion, there is no dependence on the solvent, and τ_{coll} is also 3 ps. The J-coherence anisotropies are very similar in appearance for the two gases, although they result from collision intervals which differ by a factor of 8. The most noticeable difference of the J-diffusion anisotropy is the higher dip and much longer tail.

If the collider mass in the J-coherence model is increased further, τ_{coll} must grow longer for the same $\Omega(t)$. Although the anisotropy rebound increases in height, and the final decay slows down, the coherent dip does not change and the anisotropy remains below the J-diffusion anisotropy at all time. Even in the limit $m \gg M$ ($m = 4000$ amu), τ_{coll} has only reached 2.3 ps, demonstrating the continued retention of coherence across collisions. It can be concluded from these observations that there will be density regimes for most real systems where the difference between J-diffusion and J-coherence calculations will be important.

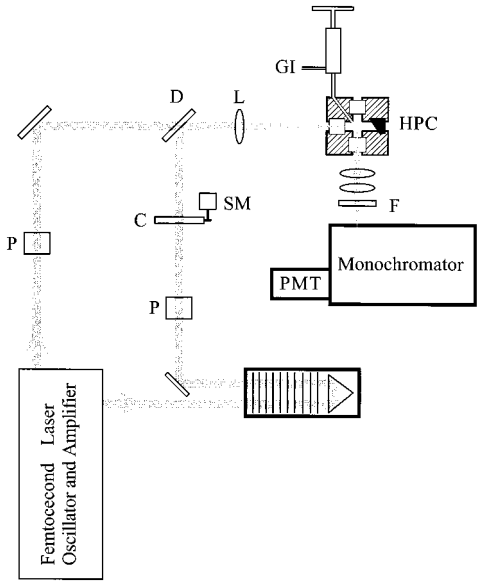

Figure 4. Experimental setup for the measurement of polarization anisotropy by pump−probe LIF of iodine in high-pressure rare gases: P, polarizer; C, Soleil compensator; SM, stepper motor; D, dichroic mirror; L, lens; GI, gas inlet; HPC, high-pressure cell; F, filter. The probe beam passes through the translation stage delay line and the compensator.

III. Experimental Section

A. Apparatus. Measurements were performed on iodine vapor at room temperature in pressures of argon or helium ranging from 0 to 3000 bar. The high-pressure apparatus has been described previously.[26] For the present studies, a new laser system was used. An amplified Ti:sapphire laser provided a train of ~700 μJ pulses of ~70 fs duration (fwhm), at $\lambda \sim 786$ nm, and 1 kHz repetition rate. A probe pulse ($\lambda \sim 393$ nm) was produced by frequency doubling a fraction of the amplified fundamental, while the remainder of the fundamental was used to pump an optical parametric amplifier. The IR output of the OPA was doubled to yield the pump pulses of center wavelength near either 613 or 622 nm. The probe beam was directed through a computer-controlled optical delay line and then colinearly recombined with the pump beam and directed into the high pressure cell (see Figure 4). With appropriate polarization and attenuation, pulse energies at the entrance to the cell were typically ~3−8 μJ for the pump and 1−3 μJ for the probe.

The pump pulse excited the ground state I_2 molecules to the B state, from which the probe pulse could subsequently induce transitions to the ion-pair-state manifold (see Figure 5). Fast collisional relaxation is known to occur to the lowest state within this manifold, the D′ state, which then fluoresces to the A′ state.[27] Fluorescence was collected perpendicular to the direction of beam propagation through a 0.5 m monochromator and detected by a PMT. Scattered pump light was further reduced by use of a UV pass interference filter. The detection wavelength was tuned to the peak of the D′ → A′ fluorescence band, which varies from 342 to 370 nm as a function of solvent species and pressure, due to solvation of the ion-pair D′ state. Signals from the PMT and a photodiode which monitored pump pulse intensity were time-gated and averaged by a boxcar integrator, and their ratio was recorded as a function of pump−probe time delay. To reduce the occurrence of temporally displaced signals that were observed to arise from specular back-reflection off each surface of the cell exit window, this window was replaced by a plug designed to serve as a beam dump.

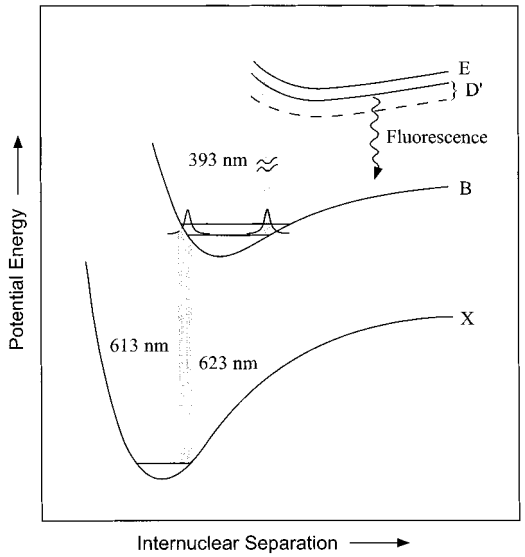

Figure 5. Schematic potential energy diagram of the iodine molecule indicating the pump−probe-LIF sequence employed for anisotropy measurements of iodine in supercritical rare gases. The lowering of the energy of the D′ state by solvation, as represented by the dashed line, varies with rare gas species and density.

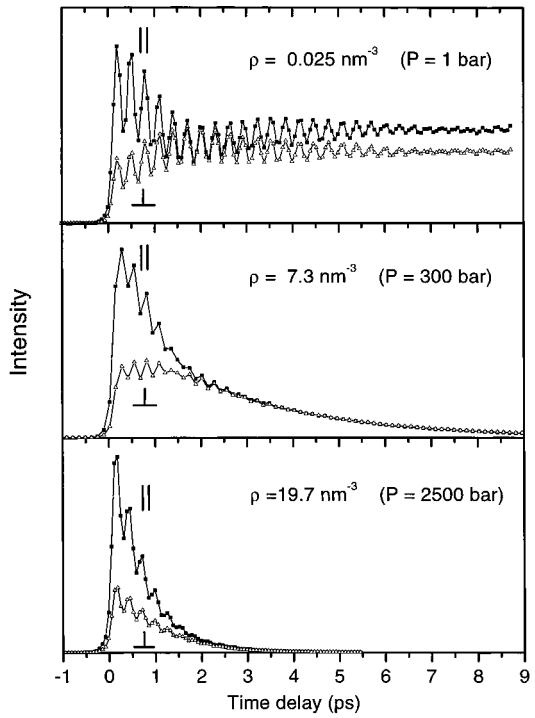

Figure 6. Experimental polarization-resolved transients of iodine in argon at the densities and pressures indicated. For all three, $\lambda_{pump} \sim$ 622 nm and $\lambda_{probe} \sim$ 394 nm.

For these studies of the time evolution of the spatial alignment of B-state population, pump and probe beams were both linearly polarized by passage through high-quality Glan-laser prism polarizers (extinction ratio 10^{-5}) and the probe polarization adjusted to be either parallel or perpendicular to that of the pump, yielding transients $I_{||}$ and $I_{\perp}$, respectively (see Figures 6 and 7). Through the course of these experiments, several different arrangements were employed to achieve the probe polarization adjustment. Since the principal uncertainties in the experimental anisotropy at a given pressure are those introduced by laser power fluctuations or drifts, or temporal shifts between parallel and perpendicular transients, the optimized arrangement,

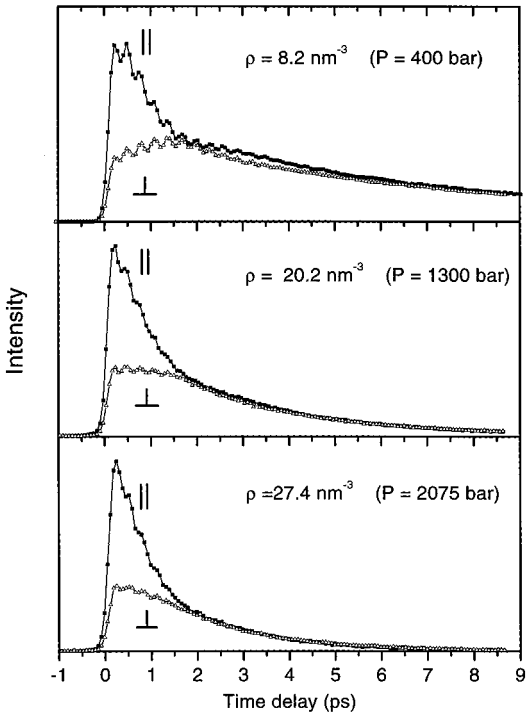

Figure 7. Experimental polarization-resolved transients of iodine in helium at the densities and pressures indicated: top, $\lambda_{pump} \sim$ 620 nm and $\lambda_{probe} \sim$ 394 nm; center and bottom, $\lambda_{pump} \sim$ 613 nm and $\lambda_{probe} \sim$ 393 nm.

as represented in Figure 4, entailed use of a Soleil compensator set to serve as a half-wave plate for the probe wavelength and mounted on a computer-controlled rotation stage. Twenty to 40 pairs of single scans (duration ∼1 min each) in alternating parallel and perpendicular configuration were then recorded and averaged to produce a matched pair of $I_{||}$ and $I_{\perp}$ transients.

The transients were experimentally checked (by measuring transients in polarization-resolved fluorescence) for potential influence of the polarization of the detected fluorescence caused by ion-pair state alignment, and none was found. This is understandable at nonzero pressures, for which the time scale of fluorescence emission is much longer than that of rotational scrambling by collisions. Therefore, as a further assurance of isotropic fluorescence, measurements were performed with a minimum buffer gas pressure of 1 bar.

B. Data Analysis. As in ref 11, data sets were analyzed by least-squares fitting to collisional model calculations of the experimental polarization anisotropy, $r(t) = (I_{||}(t) - \alpha I_{\perp}(t-t^*))/(I_{||}(t) + 2\alpha I_{\perp}(t-t^*))$, in order to extract the model collision interval, τ_{coll}. For this paper, the fitting procedure was refined, and all data were reanalyzed. A total of four adjustable parameters were used in the fitting: (1) τ_{coll}; (2) a normalization factor α to account for experimentally induced intensity variations; (3) a time shift t^* of the perpendicular transient; and (4) t_0, the zero of the time delay axis or time at which pump and probe pulses coincide in the sample. α was included as a fitting parameter because its value depended sensitively on experimental conditions. For the experimental setup shown in Figure 4, α was determined by the variation of the reflectance of the dichroic mirror (D) with polarization of the probe laser and was expected to remain constant for a given series of experiments at fixed alignment. Thus, its constancy in such a series serves as an important indicator of the success of the fitting.

When fitting the data without the third parameter, large peaks in the weighted residual were commonly observed to coincide

with the transient rises. These are symptomatic of a small misalignment of the time axes of parallel and perpendicular transients. Refitting with a floating relative temporal alignment parameter largely eliminated such anomalies in the residuals by shifts of $\leq$20 fs for over 95% of all experimental anisotropy data sets. The general evolution of the anisotropy is not sensitive to such small shifts, but their presence can severely influence the fit results, as parameters are optimized specifically to minimize the residuals of the few points on the rise which dominate the χ^2 sum. In some cases, oscillations matching the vibrational oscillations of the transients were also detected in the residuals or were visible directly in the anisotropy, and these can be caused by the same small shift between polarizations. The source of these shifts is apparently a systematic change in optical path caused by rotation of the compensator or some lens or window birefringence. This is consistent with the fact that the shift values derived from the fits remained fairly constant within any given series of experiments performed over the course of several days.

The fourth fitting parameter is t_0, the point of zero time delay between pump and probe pulses. As seen in Figure 5, at t_0 the vibrational wave packet is prepared at the inner turning point of the B-state potential, while the probe window is at or near the outer turning point. Thus, the rise of the signal induced by the probe is delayed from t_0. The time evolution of the anisotropy begins at the instant of creation of the initial sample alignment, however, and therefore a correct fit of the anisotropy yields a value of t_0, independent of the time at which the population is probed. The relationship of t_0 to the rise of the transient can depend only on the pump and probe wavelengths, the energy of the ion-pair state reached in the probe transition, and the pulse shapes and molecular response. Thus, as for α, consistency under fixed experimental conditions of the values of t_0 serves as a significant test of the quality of the fitting.

The results of the fitting were also sensitive to the form of weighting used in evaluating the best fit criterion. The weighting was propagated from the noise of the original fluorescence transients by assuming a simple model of two noise components: one independent of fluorescence intensity and one proportional to the intensity. The coefficients were determined by examination of the intensity dependence of the noise in several transients and held fixed at those values. The background intensity of each transient was fixed by an average over the measured baseline at negative time. The weighted residuals were examined for randomness as the primary indicator of a satisfactory fit.

Fits to determine the Langevin friction coefficient $1/\tau$ from eq 13 were carried out on the experimental anisotropies with α, t^*, and t_0 given by the collision model fits. Since the calculation assumes a constant rotational temperature T, while this value ranges from 220 K up to 296 K as a function of delay in each experiment, T was included with τ as a fitting parameter. The same fit weighting was used as with the collision model fitting.

The convolution of the molecular response with the cross-correlation of pump and probe pulses was tested for a response width of up to 230 fs fwhm and found to have a negligible effect ($\Delta r < 0.003$) on the more slowly evolving $r(t)$ in these experiments. Convolution was therefore disregarded in the analysis, and no efforts were made to minimize the pulse widths at the sample, which varied depending on the OPA alignment and configuration of optical elements for polarization adjustment.

IV. Results

Anisotropy measurements were performed in two distinct pump wavelength ranges in both argon and helium. At pump wavelengths of 622 $\pm$ 2 and 613 $\pm$ 2 nm, iodine is excited primarily from the $v'' = 3,4$ levels of the X state into B, $v' = 7-9$ and $v' = 9-11$, respectively. A selection of pairs of pump−probe transients in the two solvents (Figures 6 and 7) shows the range of temporal profiles observed as the pressure was varied. The differing amplitudes of vibrational oscillations (period ~300 fs) are due principally to different pulse widths. The B-state lifetime shortens dramatically at high solvent density due to collision-induced predissociation.[28] Thus, the range of time delay for which the anisotropy could be determined to high signal-to-noise grows progressively shorter as the solvent pressure increases. However, the weighting applied allowed the full transients to be included in the fits.

Collision intervals according to the J-diffusion and J-coherence models were extracted from all data sets as described in the previous section. Examples of J-coherence fits for data ranging from low to high densities are shown in Figure 8 for argon and Figure 9 for helium, with the resulting values of τ_{coll}. In the 622 nm experiments, data were acquired as described in section III, by alternating parallel and perpendicular single scans, and the normalizations were in the range 0.85−1.05, dependent on the experimental arrangement. For experiments under fixed conditions, variations were usually within $\pm$2%. For the 613 nm experiments, parallel and perpendicular transients were recorded consecutively, so the normalization varied more widely, especially with slow changes in cell transmission due to window burning or adjustments in monochromator slit width. The data acquisition rate also differed at the two pump wavelengths, so different sets of constants were determined to define the fit weighting.

The collision rates ($1/\tau_{coll}$) in argon and in helium determined from J-coherence and J-diffusion fits are plotted in Figures 10 and 11 as a function of number density. (The J-diffusion rates can be seen more clearly in Figures 12 and 13.) The densities are determined from measured pressures using experimental density/pressure data.[29,30] Also shown are calculated hard-sphere ideal-gas collision rates and Enskog hard-sphere collision rates. Both of these are equal to $1/\tau_{coll} = \pi\bar{\sigma}^2\rho\bar{v}_r\, g(\bar{\sigma})$,[31] where $\bar{\sigma}$ is the collision radius and $\bar{v}_r$ is the mean relative velocity $[8kT(\pi\mu)^{-1}]^{1/2}$ (for reduced mass μ of solvent and solute). $g(\bar{\sigma})$, the radial distribution function at contact, is equal to 1 for an ideal gas, while the Enskog value of $g(\bar{\sigma})$ for a solute at low concentration in a solvent of hard-sphere diameter σ_s has been given by Schweitzer and Chandler[32] and may be expressed in terms of the parameter $y = \rho\pi\sigma_s^3/6$ (fractional occupied volume) as

$$g(\bar{\sigma}) = \left[1 + \left(1 - \frac{3\sigma_s}{2\bar{\sigma}}\right)y + \frac{\sigma_s}{2\bar{\sigma}}\left(-1 + \frac{\sigma_s}{\bar{\sigma}}\right)y^2\right]/(1-y)^3 \quad (23)$$

The value of $\sigma_s = 2.16$ Å used for helium was derived by reproducing the experimental compressibility[29] using the Carnahan and Starling equation of state.[33] This value of σ_s implies an iodine atom diameter of 3.98 Å, given the iodine−helium $\bar{\sigma}$ of 3.07 Å. The argon density/pressure data are not well-represented by hard-sphere behavior due to a substantial attractive well, so the argon diameter is taken to account for the difference in $\bar{\sigma}$ between iodine−helium and iodine−argon with a fixed iodine diameter. This leads to a value of σ_s for argon of 3.06 Å.

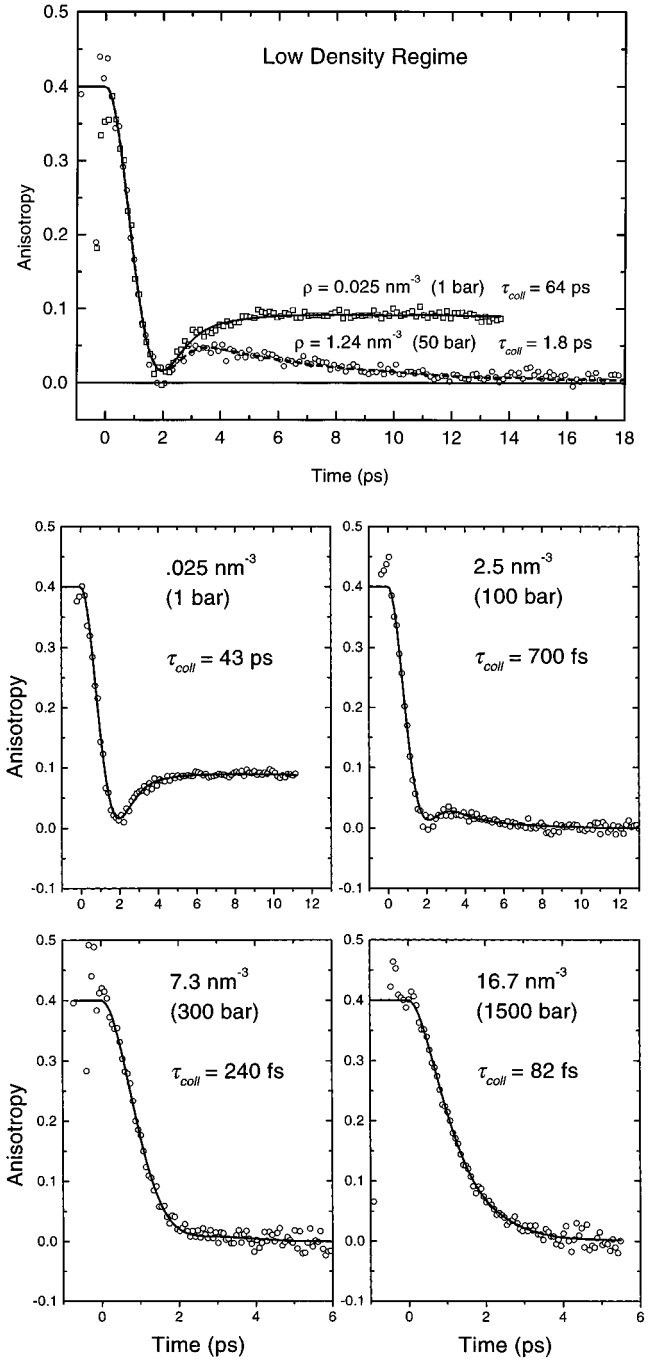

Figure 8. J-coherence fits of experimental polarization anisotropies of iodine in argon. The number density of the solvent and the J-coherence collision time are shown for each anisotropy. (a) The effect on the long time asymptote at low density; λ_{pump} = 623 nm. (b) Examples of the qualitatively distinct anisotropy functions observed by varying solvent density; λ_{pump} is 613 nm for the 300 bar data and 623 nm for the other three.

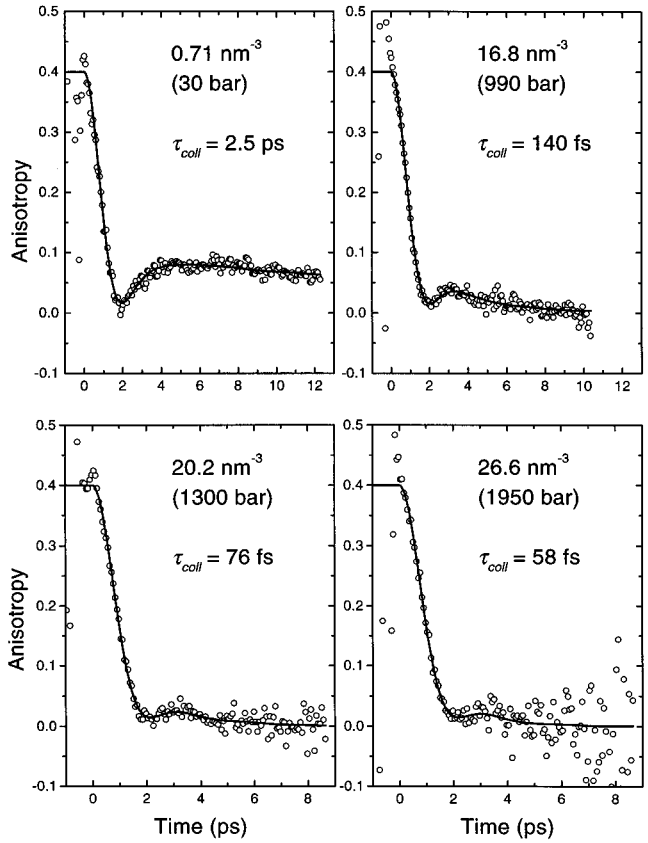

Figure 9. J-coherence fits of experimental polarization anisotropies of iodine in helium at a range of densities. The number density of the solvent and the J-coherence collision time are shown for each anisotropy. λ_{pump} is 623 nm for the 990 bar data and 613 nm for the other three.

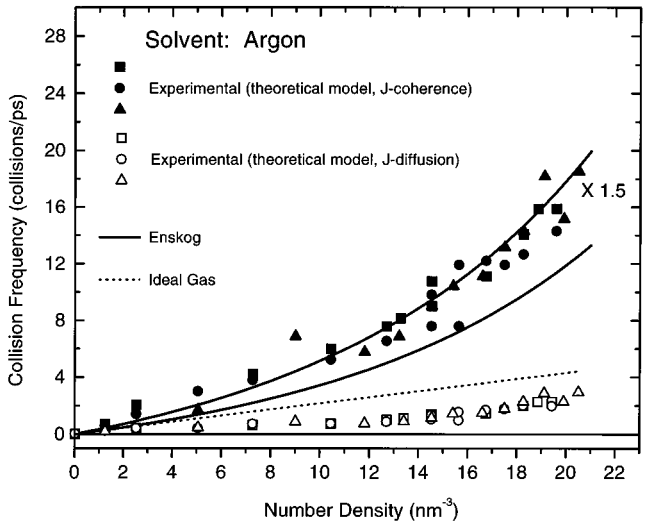

Figure 10. Solvent density dependence of the collision rates of iodine in argon derived from experimental anisotropies by the two collision models discussed in the text. Different symbols correspond to independent series of experiments. The hard-sphere ideal-gas and Enskog collision rates are shown for comparison. The Enskog curve is plotted a second time scaled by a factor of 1.5.

V. Discussion

Looking at the anisotropy decays of Figures 8 and 9, one sees that the general features of the experimental anisotropies across the full range of densities are well-reproduced by the theory. The free-rotor anisotropy, characterized by a coherent dip (at which the average rotor is approximately perpendicular to its initial direction) followed by a gradual return to the asymptotic value of 0.1, is approximated by the 1 bar argon measurement in Figure 8. The position of the dip is fixed by the angular momentum distribution and the moment of inertia of the rotor, and the dip minimum at ~2 ps corresponds to the cold J distribution at t_0^+ (see section IIA) and I of the B, $v' = 9$ state. The asymptotic value reached in the absence of collisions is due to the stationary sine-squared distribution of $\vec{J}$ with respect to the pump polarization vector. $r(t)$ clearly reflects the ||,|| pump−probe dipole sequence. (The uncertainty in

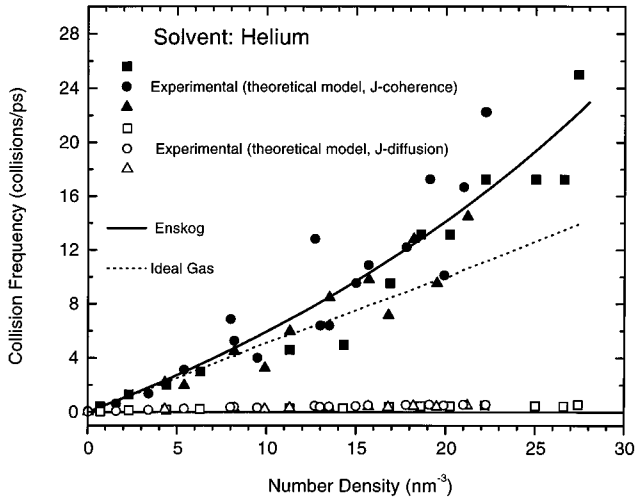

Figure 11. Solvent density dependence of the collision rates of iodine in helium derived from experimental anisotropies by the two collision models discussed in the text. Different symbols correspond to independent series of experiments. The hard-sphere ideal-gas and Enskog collision rates are shown for comparison.

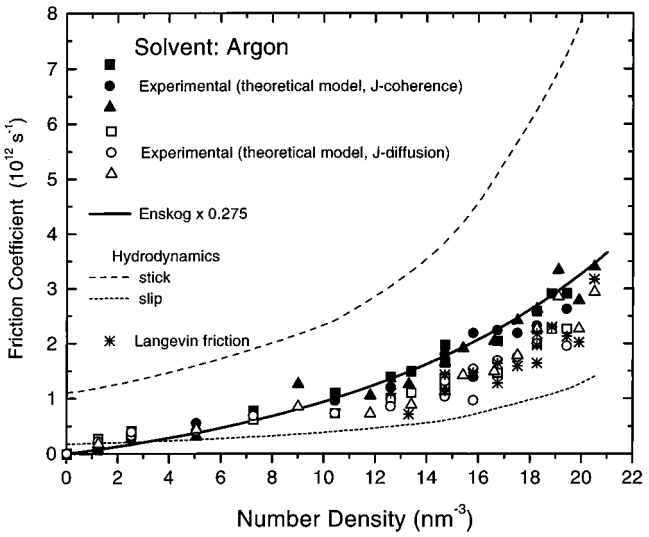

Figure 12. Density dependence of the reduced friction coefficients of iodine in argon, derived from the J-coherence and J-diffusion models, and the Langevin model (eq 13). The hydrodynamic friction for stick and slip boundary conditions is calculated as described in the text. The solid line is the Enskog collision rate scaled by 1.5/5.45 = 0.275.

values of τ_{coll} at 1 bar is large, since the real effect of collisions on the time scale of the experiments is within the noise.)

With the increase of solvent pressure, collisions with bath molecules begin to raise the rotational temperature and cause a loss of $\vec{J}$ alignment. At sufficiently low pressures, the coherent inertial motion changes little over times sufficient for angular excursions of significant fractions of 2π, so that the anisotropy dip remains clearly visible, but the long time anisotropy decays to 0 at a rate that increases with the pressure (50 and 100 bar of argon, Figure 8, and 30 and 990 bar of helium, Figure 9). The initial anisotropy decay is subject to competing effects, in that collisions lengthen the angular path the rotor axis must traverse to reach perpendicularity but raise the average angular velocity. The first effect would move the dip to later time while the second would move it to earlier time. For this reason, the dependence of the initial decay on τ_{coll} is weaker than would be the case if the internuclear distance did not change from X state to B state.

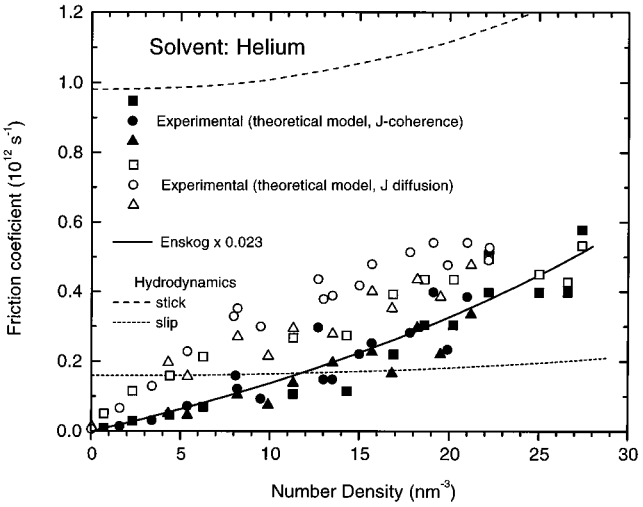

Figure 13. Density dependence of the reduced friction coefficients of iodine in helium, derived from the J-coherence and J-diffusion models. The hydrodynamic friction for stick and slip boundary conditions is calculated as described in the text. The solid line is the Enskog collision rate scaled by 1/43.4 = 0.023.

At higher pressures, the dip is gradually washed out when collisions scramble the angular momentum before the initial *dipole* alignment is totally lost (first $^1/_4$ period of rotation). At very high pressures, the dipoles undergo a relatively slow monotonic angular diffusion toward isotropy, reflected by an exponentially decaying $r(t)$. The data in Figures 8 and 9 illustrate very clearly, however, that the transition from low- to high-pressure limits has a very different density dependence in the two solvent gases. For example, the anisotropy dip has completely vanished by a density of 7.3 argon atoms/nm^3 (300 bar). Above this pressure of argon, it is possible to obtain a good fit of the anisotropy using the Langevin friction model and eq 13. The friction coefficient is not well determined, however, since the decay is essentially Gaussian, corresponding to the short-time, friction-independent limit of eq 15. In contrast, the anisotropy dip in helium is still very evident at 20 atoms/nm^3 (1300 bar). Even at 26.6 helium atoms/nm^3, a fit to the monotonically decaying anisotropy of the Langevin friction model shows a significant deviation in the residual for delays of 2−4 ps, indicating the survival of coherence of rotational motion to this time. At 16.7 nm^{-3} in argon, the anisotropy is approaching exponentiality,[11] while at the highest densities reached in helium, the anisotropy is clearly nonexponential.

J-diffusion anisotropy fits converge to the same temporal profiles in the low- and high-density limits, though the extracted collision rates are much lower, as shown in Figures 10 and 11 and discussed in section II. In the intermediate-density regime, Figure 3 shows that the two models give quantitatively different behaviors, especially in their long time asymptotic approaches to $r(t) = 0$. When the normalization α is floated in fitting this data, α values at intermediate densities are typically 3−5% lower for J-diffusion than for J-coherence fits, in order to compensate for this difference. A slightly greater emphasis on the experimental control of α than in the current data could permit a clear distinction to be made between the two types of long time decay. Presently, the difference in fit quality results predominantly from the ability to reproduce the detailed structure of the anisotropy up to ∼4 ps. After refitting all data in a consistent manner to the two models, the fit quality differed significantly ($\Delta\chi^2_r$ > 10%) for 39 out of 90 anisotropies, with J-coherence giving the better fit in 29 of those cases.

The anisotropy fits also provide a measurement of t_0. In a preliminary effort to compare the experimental t_0's to the phase of vibrational oscillations of the transients, no consistent relationship was found. However, a pattern did emerge in the t_0 values as measured relative to the midpoint in the rise of the parallel transient. This point would be fixed in time, independent of the pulse cross-correlation, in the case of a step-function molecular response. For the actual molecular responses, as seen in Figures 6 and 7, it is taken as an approximation only. For the series of experiments for excitation near 613 nm, the mean values of t_0 were -36 fs for argon (number of anisotropy measurements, $n = 13$, rms deviation of t_0, $\sigma = 18$ fs) and ~ -64 fs for helium ($n = 13$, $\sigma = 10$ fs), for a weighted average of -54 fs. For series of comparable quality at $\lambda \sim 622$ nm, the mean values were -102 fs for argon ($n = 21$, $\sigma = 27$ fs) and -89 fs helium ($n = 12$, $\sigma = 10$ fs), with weighted average -93 fs.

These results are consistent with the general trend expected from consideration of Figure 5. First, the transient rise is delayed with respect to t_0. Second, if the probe wavelength opens a Franck−Condon window near the turning point of the wave packet prepared by the 623 nm pump pulse, the 613 nm wave packet will reach the window first due to its higher velocity across the vibrational potential well. A classical calculation of vibrational trajectories at appropriate energies from their respective inner turning points to $r = 3.39$ Å (outer turning point at 623 nm) gives delays of 121 fs at 613 nm and 155 fs at 622 fs. The difference in these values of 34 fs is close to the average difference in experimental delays from t_0 to the transient midrise of 39 fs. Although the calculation is done on an approximate potential, the half-period of vibration is within 5 fs of the known value at $v' = 8$, $J = 51$. A comparison of the absolute values of the calculated and experimental delays is not warranted without a detailed analysis of the transient waveforms. Further characterization of this behavior offers a fruitful avenue of investigation of the temporal properties of pump−probe signals, which displayed some unexplained features in a recent ZEKE study of iodine with carefully determined t_0.[34]

In addition to accurately reproducing the temporal evolution of the anisotropy, a primary goal of the J-coherence model is to be able to predict its dependence on the properties of the solvent. In Figures 10 and 11, the Enskog hard-sphere collision rates are shown as derived independently of the experiments. For helium, in which collisions with iodine are well-represented by a hard-sphere potential, the experimental J-coherence collision rate is in very good agreement with the Enskog rate, within experimental uncertainty over the entire density range. The rates in argon are consistently higher than the Enskog rates, showing good agreement with a scaling of the rates by a factor of 1.5. The rates determined from molecular dynamics calculations[35] (which were plotted in Figure 4 of ref 11) show the density dependence of collisions in pure argon, based on the decay of the argon translational velocity autocorrelation function. These are close in magnitude to the J-coherence iodine−argon collision rate, but may not be quantitatively compared to them due to differences in collision potentials and relative velocity.

In the preceding comparison of J-coherence rates with Enskog rates, the lack of precise agreement in the argon data is not surprising, considering the sensitivity of the Enskog rates to the choice of model parameters $\bar{\sigma}$ and σ_s. Rather, the fundamental point that should be emphasized is that even the unrefined Enskog estimate of the gas kinetic collision rate would permit prediction to close to experimental precision of both the solvent and the density dependence of the transient anisotropies displayed in Figures 8 and 9, by J-coherence calculations. This is not possible with the J-diffusion model, for the reasons discussed in section II.

Both J-coherence and J-diffusion, as models of molecular rotation, associate a $\Omega(t)$ with each $r(t)$. Thus, we also obtain $\Omega(t)$ from the fits, and its decay rate τ determines ξ by analogy with the Langevin equation result ($\tau = 1/\xi$). In Figures 12 and 13, the fitting results are plotted in the form of friction coefficient versus density for argon and helium. For comparison, the limiting cases of hydrodynamic friction and fits to the Langevin model (eq 13) are also shown (see below). The solid curves in the figures are scaled plots of the respective Enskog collision rates. This is the form of the density dependence that is expected in the diffusion limit, where $\xi \propto 1/D_r$,[36] when the rotational diffusion coefficient D_r is assumed proportional to the Enskog translational diffusion coefficient. Note that the friction coefficient of argon is $\sim 8-10$ times larger than that of helium at equal density.

We first note from these figures that the friction coefficients determined from the two collision models, and from the Langevin model also shown for argon, are similar in magnitude, indicating the general kinematic relationship between angular displacement and angular velocity that transcends the details of the dynamics or nature of the collider and links the form of the anisotropy to that of $\Omega(t)$. Nonetheless, systematic differences in the density dependence of friction given by the two collision models do clearly reflect the details of the dynamics. For both helium and argon, the ratio of J-coherence to J-diffusion friction increases by roughly a factor of $3-4$ over the density range studied. It is interesting that the J-diffusion friction shows a faster rise at low density and then drops back to be less than or equal to the J-coherence friction at the highest densities. The J-coherence results appear more consistent with Enskog curves over the entire density range.

The results of a selection of fits to Langevin theory are shown for all densities for which a meaningful value of the friction coefficient can be derived. An example of such a fit from ref 11 is reproduced in Figure 14, showing also the different limiting forms and comparing with other relevant temporal functions. The friction values plotted in Figure 12 resulted from refitting as described in section III for consistent comparison with the collision model fits. The rotational temperatures obtained range from 230 to 290 K, consistent with a compromise between the low rotational temperature at early time and the thermalization induced by collisions. Only at the highest helium density was the Langevin fit satisfactory, but the friction coefficient was not well-determined. In argon, the Langevin friction is reasonably well determined above a density of ~ 12 nm^{-3}. The lifetime of $\Omega(t)$ at this density is of the order of 1 ps, and the collision interval is ~ 160 fs. Thus, the Langevin theory continues to fit the anisotropy and give values of the friction in close agreement with the results of the collisional models, until the correlation of the angular velocity survives over an angular trajectory of $\sim 50°$ for the average molecule. This angle for coherent motion is much larger than the expected range of validity for small-angle stochastic models.

At the highest density in helium, τ is still >1.6 ps, corresponding to a roughly 90° rotation during the correlation lifetime. The helium results are thus perfectly consistent with the range of validity of the Langevin theory observed for the argon data. This shows clearly that the proper comparison must be based upon the correlation time τ and not the collision time, which reaches ~ 40 fs in helium. In 40 fs, the average molecule

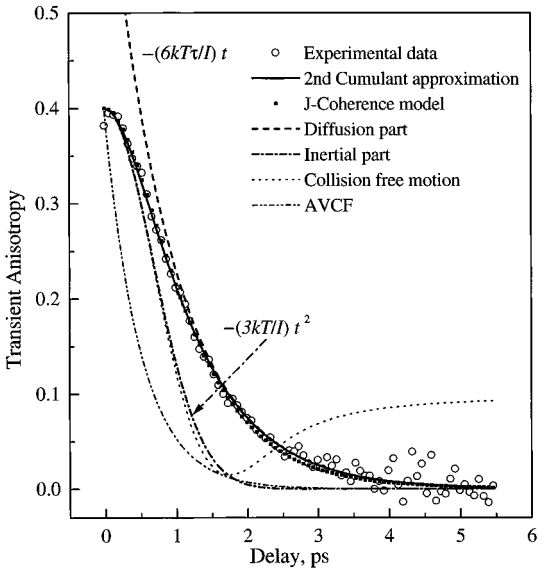

Figure 14. Illustration of a Langevin theory fit to experimental polarization anisotropy (iodine in 1500 bar supercritical argon) from ref 11. The long and short time limiting behaviors of the cumulant approximation (eq 13) are represented by the two labeled curves, where the labels are the appropriate exponents in the expressions $r(t) \propto e^x$. AVCF is the angular velocity autocorrelation function, normalized to 0.4 at $t = 0$. The corresponding J-coherence fit and free rotor anisotropy are also shown.

rotates only ∼2°, well within the range of a small angle approximation, but the weak effect of each helium collision on the iodine angular velocity allows relatively free (coherent) rotation to take place over angles approaching 90°.

The hydrodynamic range, from slip to stick boundary conditions, was calculated for a prolate ellipsoid as described in section IIC. The dimensions of the ellipsoid chosen to approximate the iodine molecule were such that the semimajor axis and volume were equal to those of the hard-sphere iodine rotor used in the J-coherence model (3.54 Å and 63.9 Å^3, leading to an axial ratio of 0.585). Values for the shear viscosities of argon and helium were taken from the literature.[37−39] Substitution in eq 16 gives $\xi_{stick} = 4936\eta$ ps^{-1}, where the viscosity is in units of poise, and interpolation in Table 1 of ref 10 gives $\xi_{slip}/\xi_{stick} = 0.162$. These relations are plotted in Figures 12 and 13. In both, the experimental friction values at high density fall in the lower half of the hydrodynamic range. This correspondence demonstrates that the solvent dependence at high density is well described by the single fluid property of shear viscosity as required by the hydrodynamic theory.

In argon, the viscosity varies strongly with density, and the relationship of the experimental friction to the hydrodynamic range is fairly constant over a wide range of density. If the point at which the scaled Enskog curve crosses the slip friction curve is taken as a simple (but arbitrary) measure of the limit of validity of the hydrodynamic treatment, the lower bound in argon is found at ∼3 nm^{-3}, where the collision times from the Enskog fit are on the order of 800 fs (average free rotation: ∼40°). In helium, where the viscosity varies little with density, the lower limit of hydrodynamic validity is at much higher density (∼12 nm^{-3}) and collision rate (τ_{coll} ∼140 fs) than in argon but at similar τ (∼5 ps). These values indicate that, as for the Langevin treatment above, τ is the parameter that characterizes the transition from coherent to diffusive motion. At this τ, however, the anisotropy is actually far from the diffusive limit, as seen in Figure 3.

The range of angular velocity correlation times given by the rough hard-sphere fluid treatment of Chandler[40] was calculated in ref 11 for spheres of volume equal to that of iodine (63.9 Å^3) and $r = 3.11$ Å. This treatment applies to a pure fluid, however, and is not applicable to the case of a solute-solvent system such as iodine solvated in argon. However, the kinetic theory of Evans et al.[41] for the calculation of orientational correlation times deals with exactly this problem, as well as that of the pure fluid of rotors. This theory gives expressions for the orientational correlation time for the *l*th rank spherical harmonic for hard ellipsoids in a mixture of hard ellipsoids and hard spheres, in the high density regime ($\tau_{rot} \gg \tau$). For the case of the anisotropy ($l = 2$) of a single rotor in a bath of spheres, and using the diffusive-limit relation between τ_{rot} and ξ (see section IIB or IIC), ξ is given in eq 54 of ref 41 as

$$\xi = 3\rho V\sqrt{\frac{kT}{2\pi I}}\frac{\epsilon^2}{\sqrt{1+\epsilon}}\lambda^{1,1}_{A,D} \tag{24}$$

where V is the ellipsoid volume, and $\epsilon = (a^2 - b^2)/b^2$, for semimajor and semiminor axes of length a and b. The factor $\lambda^{1,1}_{A,D}$ is an integral over atom−diatom collision geometries which depends on the shape parameter ϵ and moment of inertia of the ellipsoid and radial distribution function at contact and reduced mass μ of the collision pair. Equation 55 of ref 41 gives the approximation for small, light solvent atoms that we use here:

$$\lambda^{1,1}_{A,D} = \sqrt{\frac{\mu b^2}{I}}\frac{g(\bar{\sigma})}{4\epsilon^2}\left\{3 + \epsilon + \frac{1}{\sqrt{\epsilon}}(\epsilon^2 - 2\epsilon - 3)\arctan(\sqrt{\epsilon})\right\} \tag{25}$$

Note that ξ as given by eqs 24 and 25 depends on density as $\rho g(\bar{\sigma})$ and so scales precisely with the scaled Enskog curves plotted in Figures 12 and 13.

Using the same iodine ellipsoid as used in the hydrodynamic calculations, and eq 23 with the appropriate σ_s for $g(\bar{\sigma})$, $\xi(\rho)$ was calculated for iodine in argon and iodine in helium. These are equal to 1/6 and 1/3.5, respectively, times the scaled Enskog curve through the corresponding J-coherence friction values (e.g., at 20 nm^{-3}, ξ is 0.53 ps^{-1} in argon and 0.092 ps^{-1} in helium). Although we used the small collider limit in these calculations, this discrepancy is similar to that found by Evans et al. (i.e., factors ranging from 1.3 to 5.6) between their theoretical values and experiment (including molecular dynamics calculations), leading to their conclusion that the kinetic theory neglects part of the frictional drag. The comparison with the present experimental values is consistent with this conclusion and indicates that the source of the discrepancy is not due to neglect of ring collisions or neglect of "chattering" collisions (multiple collisions of a single solvent and solute without intervention of a third body), both of which are common to the J-coherence treatment.

VI. Conclusion

In this work, the dynamics of rotational motion have been studied in real time in solvent environments ranging from *isolated* molecule to *liquid* densities. With femtosecond time resolution, both inertial and diffusive aspects of the motion are observed, displaying the vibrational and coherent rotational motions. Many previous studies of rotation in liquids have focused on motion on longer time scales, reaching the picosecond regime.[42,43] In these studies, only diffusive behavior manifested by exponential anisotropy decay was observed. Even

for time resolution subsequently extending into the subpicosecond domain, the anisotropy was diffusive in nature.[44] More recently, evidence of nonexponential, but monotonic, anisotropy decays at early time has been presented, using fluorescence upconversion techniques to measure the temporal anisotropy of aniline in a series of molecular solvents.[45]

In the present work, the chosen diatomic solute and monatomic solvent form a well-defined system in terms of inertial properties, transition dipoles, and potential functions, permitting relatively unambiguous comparisons with theory. The J-coherence bimolecular collision model has been developed to allow the full range of observed forms of the anisotropy decay, from free rotational motion to rotational diffusion, to be treated in a unified manner. This model provides a clear prescription for relating the hard-sphere properties of the solvent and solute to the friction. The density dependence of the coefficient of rotational friction derived from fits of experimental anisotropies is well-described, at least semiquantitatively, over the entire experimental density range for both solvents studied, starting from the Enskog hard-sphere collision frequency.

The friction coefficients obtained from J-coherence, Gordon J-diffusion, and Langevin−Einstein analyses are similar for the highest densities of argon, for which the anisotropy can be effectively described without accounting for the effects of large-angle coherent rotational motion. In contrast, the high-density limit is not reached in helium, for which all anisotropy decays are not only nonexponential but also nonmonotonic. We conclude that the density cutoff for applicability of diffusive or continuum treatments is such that the angular trajectory for average J in time $\tau = 1/\xi$ is $\sim 50°$. In other words, the coherent rotational motion is persistent for up to $\sim 50°$ (i.e., there is memory in the solute motion), and this far exceeds the small-angle assumption invoked in stochastic theories.

Because the J-coherence model explicitly treats the collisional friction, it provides the correct relationship between the rotational motion and the time scale of hard-sphere collisions, τ_{coll}. For example, the τ_{coll} values from J-coherence fits in argon ranged from a factor of ~ 2.5 to 7.5 higher than those from J-diffusion fits and from ~ 10 to 45 times higher in helium. Likewise, since the constant ratio between the hard-sphere collision frequency and the rotational friction coefficient deduced from J-coherence theory is determined explicitly from the physical properties of the solvent, the onset of the high-density regime can be predicted from knowledge of the true collision frequency.

Acknowledgment. This work was supported by a grant from the National Science Foundation and the Air Force Office of Scientific Research. We wish to thank Dr. C. Wan for setting up the femtosecond laser system and providing advice and assistance throughout the experimental stage of this work.

Appendix

The expression (eq 20) for the change in angular momentum of a hard-sphere diatom produced by collision with an atom is derived in this appendix. The collision geometry and physical parameters used in the derivation are as represented in Figure 2. The frame of reference used is that in which the diatom center of mass is initially at rest, so $\vec{v}$ is the precollision relative velocity. The final velocities are $\vec{v}'$ and $\vec{V}'$ for atom and diatom. The collision imparts an impulse $M\vec{V}'$ in direction $\hat{f}$ at the point of impact on the diatom, producing a change in angular momentum of $\Delta\vec{J} = (\vec{r}/2 - \hat{f}\bar{\sigma}) \times MV'\hat{f} = {}^1/_2 MV'(\vec{r} \times \hat{f})$.

The conservation of linear momentum in the form $\vec{v}' = \vec{v}' - (M/m)\vec{V}'$ can be used to eliminate v' from the conservation of energy

$$\frac{1}{2}mv^2 + \frac{1}{2}\frac{J^2}{I} = \frac{1}{2}mv'^2 + \frac{1}{2}MV'^2 + \frac{1}{2}\frac{J'^2}{I} \qquad \text{(A1)}$$

to give

$$\frac{1}{2}\frac{J^2}{I} = -MV'(\vec{v}\cdot\hat{f}) + \frac{1}{2}M(1 + M/m)V'^2 + \frac{1}{2}\frac{J'^2}{I} \qquad \text{(A2)}$$

and from the conservation of angular momentum

$$\vec{J} + \left(\frac{\vec{r}}{2} - \hat{f}\bar{\sigma}\right) \times m\vec{v} = \vec{J}' + \left(\frac{\vec{r}}{2} - \hat{f}\bar{\sigma}\right) \times mv' \qquad \text{(A3)}$$

to give

$$\vec{J}' = \vec{J} + \left(\frac{\vec{r}}{2} - \hat{f}\bar{\sigma}\right) \times MV'\hat{f} = \vec{J} + \frac{1}{2}MV'(\vec{r} \times \hat{f}) \qquad \text{(A4)}$$

Using eq A4 to replace J' in eq A2 yields a quadratic in the unknown V':

$$0 = -M(\vec{v}\cdot\hat{f})V' + \frac{1}{2}M(1 + M/m)V'^2 + \frac{M[\vec{J}\cdot(\vec{r} \times \hat{f})]}{2I}V' + \frac{M^2(\vec{r} \times \hat{f})^2}{8I}V'^2 \qquad \text{(A5)}$$

One solution is $V' = 0$, which corresponds to no interaction between the atom and diatom. The nontrivial solution, with the substitution $I = Mr^2/4$, is

$$V' = \frac{-Mr^2(\vec{v}\cdot\hat{f}) + 2[\vec{J}\cdot(\vec{r} \times \hat{f})]}{-\frac{1}{2}Mr^2(1 + M/m) - \frac{1}{2}M(\vec{r} \times \hat{f})^2} \qquad \text{(A6)}$$

Using $\vec{r} = r\hat{r}$, $(\hat{r} \times \hat{f})^2 = 1 - (\hat{r}\cdot\hat{f})^2$, and $\vec{J}\cdot(\hat{r} \times \hat{f}) = -(\vec{J} \times \hat{f})\cdot\hat{r}$, eq A6 can be put in the form

$$V' = \frac{Mr(\vec{v}\cdot\hat{f}) + 2[(\vec{J} \times \hat{f})\cdot\hat{r}]}{\frac{1}{2}Mr(2 + M/m - (\hat{r}\cdot\hat{f})^2)} \qquad \text{(A7)}$$

from which $\vec{v}'$ and eq 20 for $\Delta\vec{J}$ follow immediately.

References and Notes

(1) Hänggi, P.; Talkner, P.; Borkovec, M. *Rev. Mod. Phys.* **1990**, *66*, 251; Tarjus, G.; Kivelson, D. *Chem. Phys.* **1991**, *152*, 153.
(2) Berne, B. J.; Pecora, R. *Dynamic Light Scattering*; John Wiley and Sons: New York, 1976.
(3) Hynes, J. T. In *The Theory of Chemical Reaction Dynamics*; Baer, M., Ed. CRC Press: Boca Raton, 1984; Vol. 4, p 171.
(4) Edwardes, E. *Q. J. Pure Appl. Math.* **1892**, *26*, 70.
(5) Perrin, F. *J. Phys. Radium* **1934**, *5*, 497; **1936**, *7*, 1.
(6) Debye, P. *Polar Molecules* Chemical Catalog Company: 1929.
(7) Steele, W. A. *J. Chem. Phys.* **1962**, *38*, 2404, 2411.
(8) Gordon, R. G. *J. Chem. Phys.* **1966**, *44*, 1830.
(9) Eisenthal, K. B. *Acc. Chem. Res.* **1975**, *8*, 118.
(10) Hu, C.-M.; Zwanzig, R. *J. Chem. Phys.* **1974**, *60*, 4354.
(11) Baskin, J. S.; Gupta, M.; Chachisvilis, M.; Zewail, A. H. *Chem. Phys. Lett.* **1997**, *275*, 437.
(12) Mazur, P.; Oppenheim, I. *Physica* **1970**, *50*, 241−258.
(13) Mehaffey, J. R.; Desai, R. C.; Kapral, R. *J. Chem. Phys.* **1977**, *66*, 1665.
(14) Variyar, J. E.; Kivelson, D. *J. Chem. Phys.* **1992**, *96*, 593.
(15) Furtado, P. M.; Mazenko, G. F.; Yip, S. *Phys. Rev. A*, **1976**, *14*, 869.
(16) Mazenko, G. F. *Phys. Rev. A* **1973**, *2*, 209; *Phys. Rev. A* **1973**, *7*, 222.

(17) Burshtein, A. I.; Temkin, S. I. *Spectroscopy of Molecular Rotation in Gases and Liquids*; Cambridge University Press: Cambridge, 1994.
(18) Hansen, J. P.; McDonald, I. R. *Theory of Simple Liquids*, 2nd ed.; Academic Press: London, 1986. Coffey, W. T.; Kalmykov, Y. P.; Waldron, J. T. *The Langevin Equation*. World Scientific: Singapore, 1996.
(19) Kubo, R.; Toda, M.; Hashitsume, N. *Statistical Physics II*; Springer: Berlin, 1995.
(20) Kluk, E.; Powles, J. G. *Mol. Phys.* **1975**, *30*, 1109.
(21) Pomeau, Y.; Weber, J. *J. Chem. Phys.* **1976**, *65*, 3616.
(22) Lynden-Bell, R. M.; McDonald, I. R. *Mol. Phys.* **1981**, *43*, 1429.
(23) van Kampen, N. G. *Physica* **1974**, *74*, 215, 239.
(24) Li, Z.; Bormann, A.; Martens, C. C. *J. Chem. Phys.* **1992**, *97*, 7234.
(25) Schatz, G. C.; Buch, V.; Ratner, M. A.; Gerber, R. B. *J. Chem. Phys.* **1983**, *79*, 1808.
(26) Materny, A.; Lienau, C.; Zewail, A. H. *J. Phys. Chem.* **1996**, *100*, 18650.
(27) Martin, M.; Fotakis, C.; Donovan, R. J.; Shaw, M. J. *Nuovo Cimento* **1981**, *63*, 300.
(28) Lienau, C.; Williamson, J. C.; Zewail, A. H. *Chem. Phys. Lett.* **1993**, *213*, 289. Lienau, C.; Zewail, A. H. *J. Phys. Chem.* **1996**, *100*, 18629.
(29) McCarty, R. D. *J. Phys. Chem. Ref. Data* **1973**, *2*, 923.
(30) Stewart, R. B.; Jacobsen, R. T. *J. Phys. Chem. Ref. Data* **1989**, *18*, 639.
(31) McQuarrie, D. A. *Statistical Mechanics*; Harper and Row: New York, 1976.
(32) Schweitzer, K. S.; Chandler, D. *J. Chem. Phys.* **1982**, *76*, 2296.
(33) Carnahan, N. F.; Starling, K. E. *J. Chem. Phys.* **1969**, *51*, 635.
(34) Fischer, I.; Vrakking, M. J. J.; Villeneuve, D. M.; Stowlow, A. *Chem. Phys.* **1996**, *207*, 331.
(35) Liu, Q.; Wan, C.; Zewail, A. H. *J. Phys. Chem.* **1996**, *100*, 18666.
(36) Tyrrell, H. J. V.; Harris, K. R. *Diffusion in Liquids*; Butterworths: London, 1984.
(37) Vermesse, J.; Vidal, D. *C. R. Acad. Sci. B* **1973**, *272*, 191.
(38) Trappeniers, N. J.; Van Der Gulik, P. S.; Van Den Hooff, H. *Chem. Phys. Lett.* **1980**, *70*, 438.
(39) Vermesse, J.; Vidal, D. *C. R. Acad. Sci. B* **1976**, *282*, 5.
(40) Chandler, D. *J. Chem. Phys.* **1974**, *60*, 3500, 3508.
(41) Evans, G. T.; Cole, R. G.; Hoffman, D. K. *J. Chem. Phys.* **1982**, *77*, 3209.
(42) Chuang, T. J.; Eisenthal, K. B. *J. Chem. Phys.* **1972**, *57*, 5094.
(43) See: Fleming, G. R. *Chemical Applications of Ultrafast Spectroscopy*; Oxford University Press: Oxford, 1986; Chapter 6 and references therein.
(44) Millar, D. P.; Shah, R.; Zewail, A. H. *Chem. Phys. Lett.* **1979**, *66*, 435.
(45) Pereira, M. A.; Share, P. E.; Sarisky, M. J.; Hochstrasser, R. M. *J. Chem. Phys.* **1991**, *94*, 2513.